thermo

MDPI

Article

Impact of Inlet Configuration and Flow Rates on Thermal Storage Stratification and Efficiency

Aiym Kereikulova [1], Yelnar Yerdesh [1], Yerzhan Belyayev [1,*], Amankeldy Toleukhanov [2], Olivier Botella [3], Abdelhamid Kheiri [3] and Mohammed Khalij [3]

[1] Department of Mechanics, Al-Farabi Kazakh National University, Almaty 050040, Kazakhstan; aiymkereikulova56@gmail.com (A.K.)
[2] Department of Mechanical Engineering, Satbayev University, Almaty 050013, Kazakhstan
[3] CNRS, LEMTA, Université de Lorraine, F-54000 Nancy, France; olivier.botella@univ-lorraine.fr (O.B.); abdelhamid.kheiri@univ-lorraine.fr (A.K.)
* Correspondence: yerzhan.belyaev@kaznu.edu.kz

Abstract

Thermal stratification strongly affects the efficiency and operational reliability of sensible thermal energy storage (TES) tanks in energy systems. This study numerically investigates the combined influence of inlet configuration and mass flow rate on the charging performance of a vertical cylindrical TES tank (H = 3 m, D = 1 m) using transient CFD simulations. Five inlet designs—open, orifice, groove, shower, and shower-groove are analyzed at three flow rates: Q_1 = 0.0003 m^3/s, $Q_2 = Q_1/2$, and $Q_3 = Q_1/3$. System performance is evaluated using key thermal and stratification metrics. Increasing the flow rate from Q_3 to Q_1 enhances convective heat transfer and energy and exergy efficiencies, but significantly intensifies mixing and degrades thermal stratification. At Q_1, the groove inlet achieves the highest capacity ratio and exergy efficiency (0.87), while exhibiting increased mixing. Reducing the flow rate to Q_2 and Q_3 limits inlet-induced momentum, leading to improved stratification for all configurations. The shower-groove inlet reaches a maximum stratification level (tail factor) of 1.13 at Q_3, indicating superior thermal layering, albeit with lower energetic efficiency (≈0.40–0.45). The groove inlet provides the best overall compromise at Q_2, combining high efficiency with stable stratification. These results demonstrate a clear efficiency-stratification trade-off and highlight the importance of selecting inlet-flow combinations according to application-specific objectives.

Keywords: thermal storage system; inlet configuration; mass flow rate; exergy efficiency; thermal stratification

Check for updates

Academic Editor: Luisa F. Cabeza

Received: 9 December 2025
Revised: 14 February 2026
Accepted: 24 February 2026
Published: 27 February 2026

Copyright: © 2026 by the authors. Licensee MDPI, Basel, Switzerland. This article is an open access article distributed under the terms and conditions of the Creative Commons Attribution (CC BY) license.

1. Introduction

The rapid growth in global energy demand, coupled with increasing concerns related to fossil fuel depletion and greenhouse gas emissions, has accelerated the deployment of renewable energy technologies. Among these, Concentrated Solar Power (CSP) systems represent a promising option for large-scale, dispatchable renewable electricity generation, particularly when integrated with Thermal Energy Storage (TES) units. TES systems enable the decoupling of energy production and consumption, improving plant flexibility, stability, and overall efficiency, and are now considered a key component in most modern CSP installations [1–4].

Stratified sensible heat storage tanks are widely used in CSP, solar thermal, HVAC, and industrial heat management applications due to their simplicity, robustness, and cost-

effectiveness. Their performance strongly depends on the ability to maintain thermal stratification, characterized by well-defined vertical temperature layers that minimize mixing between hot and cold regions. Preserving stratification enhances energy and exergy efficiencies, reduces entropy generation, and improves the quality of the delivered thermal energy [5,6].

Among the various factors influencing stratification, inlet configuration and flow conditions play a dominant role, as they directly control the momentum distribution, jet penetration, and mixing processes inside the tank. Experimental investigations have shown that increasing inlet velocity generally promotes mixing and degrades stratification in hot water storage tanks, whereas reduced inlet momentum favors stable thermocline formation [7]. To mitigate inlet-induced mixing, various inlet devices such as diffusers, perforated plates, manifolds, and fabric-based stratification systems have been proposed [8,9]. While Altuntop et al. [7] employed an early CFD framework to analyze the influence of inlet velocity on thermal stratification, their model was limited by simplified inlet representations and a primary focus on local temperature distributions. By contrast, the present study adopts a modern ANSYS Fluent 2D axisymmetric transient CFD approach, allowing detailed resolution of multiple inlet geometries and a systematic evaluation of stratification using quantitative performance indicators. In addition, Davidson and Adams [8] experimentally demonstrated that fabric-based stratification manifolds significantly reduce inlet-induced mixing by distributing the inflow according to buoyancy forces, achieving a 4% improvement in stratification compared to rigid porous manifolds and up to 48% improvement relative to conventional drop-tube inlets under realistic operating conditions. Their results highlight the strong potential of inlet momentum control for enhancing thermal stratification, thereby motivating further CFD-based investigations of inlet geometry effects under controlled and reproducible conditions. Zachar et al. [10] employed a validated two-dimensional laminar CFD model to investigate the influence of diffuser plates on thermal stratification in vertical storage tanks with both upper and lower inlet configurations. Their results demonstrated that appropriate plate size and positioning can significantly reduce inlet-induced mixing and help preserve a stable thermocline. Abdidin et al. [11] numerically investigated the influence of an internal disk on thermocline formation in a vertical thermal storage tank and demonstrated that the presence of the disk effectively suppresses inlet-induced mixing and stabilizes the temperature stratification. Their results showed that an appropriately positioned internal disk leads to a sharper thermocline and improved stratification efficiency compared to a conventional tank configuration without internal flow control elements.

Several studies have specifically addressed the influence of inlet design on the performance of stratified thermal storage tanks. Experimental work has demonstrated that inlet structure significantly affects discharging behavior, thermal efficiency, and outlet temperature stability in solar storage tanks [12]. Li et al. [12] experimentally investigated the effect of inlet structure on the discharging performance of a solar water storage tank and demonstrated that a slotting-type inlet significantly enhances thermal stratification compared with direct and shower-type inlets. At a flow rate of 5 L·min^{-1}, the slotting-type inlet achieved an effective discharging efficiency of 90%, which is 18.4% and 26.8% higher than that of the direct and shower-type inlets, respectively, while also extending the effective discharging time by up to 26.4%. Authors employed an experimental method without resolving internal flow fields or local momentum distributions. Entrance effects and inlet jet instabilities have also been identified as critical mechanisms governing stratification degradation, particularly under high flow-rate conditions [13]. Shah and Furbo [13] combined CFD simulations and experiments to investigate entrance effects of different inlet designs in solar storage tanks and demonstrated that inlet geometry strongly governs jet penetration and stratification degradation during draw-off. At a flow rate of 10 L·min^{-1}, a

flat-plate inlet preserved up to 34% of the tank volume as deliverable hot water, compared with only 19% for a simple pipe inlet, while an ideal inlet would retain approximately 47%, highlighting the critical role of inlet momentum control. Shah and Furbo [14] combined laboratory experiments with a transient three-dimensional CFD model (CFX 4.1) to investigate heat transfer and stratification in vertical mantle tanks used in low-flow solar domestic hot water systems. They reported a maximum deviation of about 2 K for internal tank temperatures and 3 K for the mantle outlet temperature between experiments and simulations, and derived a local heat-transfer correlation with a determination coefficient of $R^2 = 0.95$, confirming that heat transfer is dominated by buoyancy-driven natural convection.

Complementary to experimental investigations, Computational Fluid Dynamics (CFD) has been widely employed to analyze inlet-induced flow structures, thermal plumes, and coherent vortical patterns in stratified tanks. CFD studies have shown that flow instabilities and coherent structures can strongly influence thermocline thickness and storage efficiency [15]. More recently, three-dimensional unsteady CFD simulations have been used to compare different inlet configurations under transient operating conditions, confirming that inlet geometry optimization remains a critical design challenge for TES systems [16]. Abdidin et al. [17] previously conducted a comprehensive three-dimensional laminar CFD investigation of a domestic hot water storage tank with various inlet and outlet configurations to assess their influence on thermal stratification, mixing behavior, and storage performance. That study focused on water as the heat transfer fluid under domestic heating conditions, whereas the present work extends this line of research to high-temperature thermal oil applications, addressing stratification behavior under substantially different thermophysical properties and operating temperature ranges.

Despite this extensive body of literature, several gaps remain. Many studies focus on a single inlet concept or a limited operating range, making direct comparison between inlet designs difficult. In addition, the combined effect of inlet geometry and mass flow rate on both energy-based and exergy-based performance indicators is not always addressed within a unified framework. Furthermore, while qualitative assessments of stratification are common, fewer studies provide systematic comparisons using multiple quantitative indicators such as capacity ratio, stratification number, MIX number, and exergy efficiency [18]. Charging and discharging efficiency are widely applied to evaluate the system's capability to absorb and release energy effectively throughout operational cycles [19,20]. The capacity ratio quantifies the fraction of useful energy stored relative to the system's total capacity, while the tail factor provides insights into the stability of discharge profiles, especially during the final stages of energy delivery [21]. Another key parameter is the stratification number, which reflects the degree of temperature stratification within the tank and is directly related to energy efficiency [6]. Exergy efficiency is also frequently employed, as it accounts for irreversibility or exergy destruction, during energy storage and recovery, thus measuring the quality rather than only the quantity of stored energy [22]. Moreover, metrics such as the Richardson, MIX and stratification numbers have been proposed to quantify thermal stratification in PCM-assisted systems [9]. The present work establishes a basis for future studies addressing inlet optimization in TES systems containing packed-bed or PCM elements. Collectively, these indicators and metrics enable a comprehensive understanding of TES systems and guide optimization strategies through adjustments in heat transfer fluid (HTF) [23] properties and operational conditions.

In this context, the present study provides a comparative CFD-based analysis of multiple inlet configurations—namely open, orifice, groove, shower, and shower-groove inlets, under different mass flow rates in a cylindrical stratified thermal energy storage tank. The focus is placed on the charging process and on evaluating the interplay between inlet-induced flow structures, thermal stratification, and energy/exergy performance us-

ing a consistent set of key performance indicators. Rather than proposing a novel inlet concept, this study provides a systematic, design-oriented comparison of selected inlet geometries to assess their influence on flow dynamics and thermal stratification under controlled conditions.

2. Materials and Methods

The present study addresses three key research questions. First, it investigates the influence of different inlet configurations on thermal stratification and energy storage performance in a stratified thermal energy storage tank. Second, it examines the effect of varying mass flow rates on the trade-off between exergy efficiency and stratification quality. Finally, the study aims to identify inlet-flow combinations that provide an optimal balance between thermal stratification and overall system efficiency.

It is hypothesized that optimized inlet geometries, such as groove and shower–groove designs, enhance thermal stratification by reducing inlet-induced mixing within the storage tank. In addition, lower mass flow rates are expected to improve stratification quality, albeit at the expense of energy storage performance. Accordingly, it is assumed that an intermediate operating regime exists in which both exergy efficiency and thermal stratification can be simultaneously optimized.

The research was conducted through a sequence of well-defined stages. First, relevant published studies were analyzed to identify existing approaches for improving the performance of thermal energy storage tanks and to clarify unresolved issues related to inlet configuration design. Second, a numerical model of a hot working-fluid storage tank was developed using ANSYS Fluent 2024 R2 (ANSYS Inc., Canonsburg, PA, USA). The modeling strategy was selected according to inlet geometry: for the open inlet and orifice-groove configurations, a two-dimensional axisymmetric model was employed to reduce computational cost while maintaining accuracy, whereas for more complex inlet designs, such as the shower and shower-groove inlets, a full three-dimensional model was adopted to resolve flow distribution and vortex structures. Third, boundary conditions were specified, including variations in mass flow rate, while the inlet temperature was kept constant, and a series of transient CFD simulations was performed. The simulation results were also compared with published experimental data [10], confirming the reliability of the adopted methodology. Finally, the results were post-processed to evaluate key performance indicators, including storage capacity ratio, exergy efficiency, tail factor, MIX number and stratification number.

The physical model for this study consists of a cylindrical thermal storage tank (of height 3 m and diameter of 1 m [17]) equipped with various inlet configurations, including open, groove, orifice, shower, and shower groove as shown in Figure 1 and Table 1. These configurations influence the distribution of the heat transfer fluid (HTF), in this case, working fluid (thermal oil), within the tank and its thermal stratification. The tank dimensions and the working fluid-properties shown in Table 2, were adopted from the works of Sougtan et al. [19].

The geometry of the thermal energy storage tank considered in this study (height = 3 m, diameter = 1 m) was selected to achieve an aspect ratio $AR = H/D = 3$, which lies within the recommended range for preserving a stable thermocline in stratified storage tanks. Previous numerical and theoretical investigations have demonstrated that tanks with moderate-to-high aspect ratios (typically $AR \approx 2.5$–3.5) significantly reduce large-scale mixing and promote sharper thermocline formation, whereas low-aspect-ratio tanks are more prone to excessive mixing and degradation of stratification quality (Karim et al., 2018 [5]). The present geometry is therefore not intended to represent a specific application scale, but rather to serve as a reference configuration that ensures physically meaningful stratifica-

tion while isolating the effects of inlet geometry and flow rate. Although dimensionless parameters such as the Reynolds number, Richardson number, and aspect ratio are useful for characterizing stratified TES behavior, the present results are primarily intended to elucidate inlet-induced flow mechanisms and stratification trends under controlled conditions, rather than to provide direct quantitative scalability across system sizes. As reported in Ref. [24], scalability limitations arise in thermocline storage tanks containing packed-bed layers. Since the present work does not consider packed-bed media or PCM containers, the conclusions are limited to single-phase storage tanks with different inlet configurations within the scope of the investigated conditions.

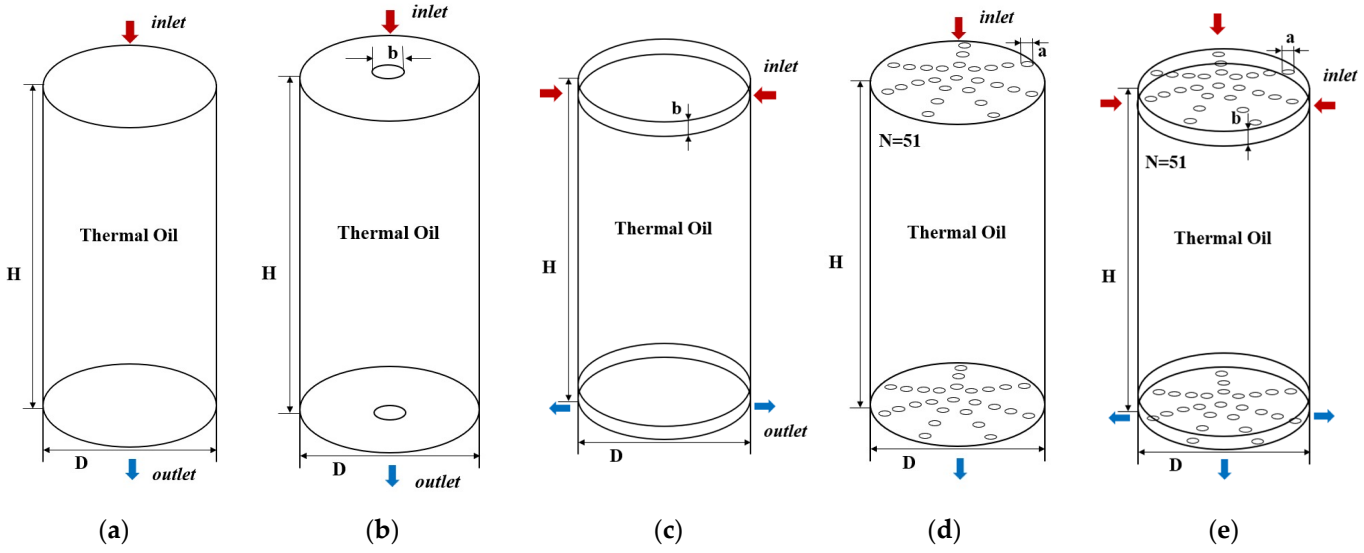


Figure 1. Various inlet configurations used for the storage tank: (**a**) open inlet; (**b**) orifice inlet; (**c**) groove inlet; (**d**) shower inlet; (**e**) shower-groove inlet. The last two configurations contain $N = 51$ holes (tank dimensions: $H = 3$ m, $D = 1$ m).

Table 1. Dimensions of the various inlet configurations displayed in Figure 1.

Inlet Types	b (m)	a (m)
Open inlet	1	
Orifice inlet	0.1	
Groove inlet	0.09	
Shower		0.03 (N = 51)
Shower Groove	0.09	0.03 (N = 51)

Table 2. Properties of working fluid.

Properties	Value
C_p (Specific Heat) [J/(kg·K]	2055.8
Thermal conductivity [W/(m·K)]	0.1194
Viscosity [kg/(m·s)]	0.0012
Thermal expansion coefficient [1/K]	0.000819
Density [kg/m^3]	921.7

The simulations focus on the charging process, with an inlet temperature of 523 K and an initial temperature of 373 K. The mass flow rate of the HTF is kept constant, and the flow velocity adjusted to the various inlet configurations of Figure 1. The flow rates Q_1 = 0.0003 m^3/s (as in [19]), $Q_2 = Q_1/2$ and $Q_3 = Q_1/3$ have been considered, in order to investigate the impact of varying Q on the thermal performance and stratification within the tank. In the shower-groove configuration, the calculated flow distribution indicates

that approximately 88.7% of the total flow passes through the groove section, while 11.3% is distributed through the shower openings. The use of three different mass flow rates also allows to identify possible nonlinearities in the system behaviour, to assess the stability and reproducibility of the results, and to get a better understanding of the dynamics of the measured parameters.

The model assumes that the tank walls are perfectly insulated, preventing any heat loss to the surrounding environment. This idealized assumption is crucial for accurately evaluating the thermal efficiency of the system.

2.1. Governing Equations

The unsteady flow models for heat transfer within a standard storage tank are based on the following assumptions:

- incompressible working fluid (thermal oil);
- thermophysical properties are constant;
- Newtonian fluid behaviour;
- negligible viscous dissipation effects;
- laminar fluid flow.

In addition, buoyancy effects modelled by the Boussinesq approximation are not included, since our CFD model is intentionally formulated to isolate inlet-induced forced convection mechanisms and their influence on flow structure and stratification. Under these assumptions, the continuity equation can be written as:

$$\nabla \cdot \vec{u} = 0, \tag{1}$$

The momentum equation is:

$$\frac{\partial \vec{u}}{\partial t} + \left(\vec{u} \cdot \nabla\right)\vec{u} = -\frac{1}{\rho_0}\nabla P + \vartheta \nabla^2 \vec{u}, \tag{2}$$

and the energy equation governing the heat exchange process is expressed:

$$\rho_f C_{p_f} \frac{\partial T}{\partial t} + \rho_f C_{p_f} \vec{u} \nabla T = \nabla (k \nabla T), \tag{3}$$

where $\vec{u}$ is the velocity vector, P is pressure (Pa), ρ_0 is the reference density (kg/m^3), ϑ is kinematic viscosity (m^2/s), ρ_f is fluid density (kg/m^3), C_{p_f} is specific heat capacity (J/(kg·K)), T is temperature (K), k is thermal conductivity (W/(m·K)), and t is time (s).

According to the Reynolds number based on the characteristic inlet velocity, the flow regime in the present study can be reasonably classified as laminar for the investigated inlet configurations. The calculated Reynolds numbers are Re = 294 for the open inlet, Re = 146 for the groove inlet, Re = 192 for the shower inlet, and Re = 130 (groove part) and Re = 22 (shower part) for the combined groove-shower configuration. All these values remain well below the commonly accepted laminar-transition threshold of Re $\approx$ 2300 for internal flows. Only the single-orifice inlet yields a higher Reynolds number (Re = 2933), corresponding to a transitional regime. However, this configuration is considered solely as a hypothetical reference case to assess the sensitivity of the system to elevated inlet momentum and is not intended to represent a practical operating condition. Given that the dominant flow conditions across the investigated inlet designs fall within the laminar regime, and in order to maintain methodological consistency and enable direct comparability among all cases, a laminar flow formulation was employed throughout the study.

As initial condition, the working fluid in the tank is at rest at a temperature set to 373 K. At the inlet boundary, a constant flow rate (discussed previously) and temperature

of 523 K are applied, while the outlet pressure is set to zero. The simulation is stopped once the outlet temperature reaches the desired value for full charge, specifically when the bottom-outlet temperature reaches 493 K.

2.2. Performance Indicators

The *capacity ratio* $\sigma \in [0, 1]$ is a key metric that reflects the proportion of thermal energy stored or released relative to a tank's maximum energy storage capacity. A ratio of 1 indicates complete charging or discharging, meaning the tank is fully utilized. When σ is less than 1, only a portion of the tank's capacity is used, which may occur under partial load conditions. The capacity ratio is crucial for assessing the efficiency of thermal storage systems, indicating whether the tank is being used optimally or if unused capacity could be better utilized. The capacity ratio is defined as:

$$\sigma = \frac{E_{stored}}{E_{\max_stored}}, \tag{4}$$

where

$$E_{stored} = \int_V \rho_f C_{p_f} (T - T_c) dV, \tag{5}$$

and:

$$E_{\max_stored} = \rho_f C_{p_f} V_{tank} (T_h - T_c), \tag{6}$$

with T is the current working fluid temperature, T_h, T_c are hot and cold working fluid temperatures. C_{p_f} and ρ_f are working fluid specific heat and density, respectively, V_{tank} is the tank volume, E_{stored} is the current stored energy, and $E_{\max_stored}$ is the tank's maximum storage capacity.

Exergy which is derived from the first and second laws of thermodynamics, measures both the quantity and quality of thermal energy. It evaluates the potential for available useful work based on the temperature difference between the stored fluid and the environment. Exergy efficiency $\eta_{exergy} \in [0, 1]$, as defined by [25], is the ratio of current stored exergy to the maximum achievable exergy at the end of the charging process, reflecting how close the system is to optimal performance:

$$\eta_{exergy} = \left. \frac{Exergy_{real}}{Exergy_{ideal}} \right|_{end\ of\ charging\ process}, \tag{7}$$

where:

$$Exergy_{real} = \int_V \rho_f C_{p_f} (T - T_a) dV - \int_V \rho_f C_{p_f} T_a ln\left(\frac{T}{T_a}\right) dV, \tag{8}$$

and

$$Exergy_{\text{ideal}} = \rho_f C_{p_f} V_{tank} \left[(T_h - T_a) - T_a ln\left(\frac{T_h}{T_a}\right) \right], \tag{9}$$

with T_a the ambient temperature. $\eta_{exergy} \in [0, 1]$ is the exergy efficiency, T_a is the ambient temperature (298 K), and other symbols are as defined in Equations (7)–(9).

The *tail factor* $\in [0, 1]$ is based on the temperature profile of the HTF as it exits the storage system over time. Its main advantage is that it does not depend on the thermal properties of the HTF, system geometry, or specific operational conditions, making it a reliable metric for evaluating the quality of stored thermal energy. This independence allows for easy comparison between different storage systems, enabling engineers to objectively assess and optimize performance across various designs [26].

The tail factor ε_{ch} is defined by the ratio between the dimensionless outlet temperature (T_{out}) with respect to dimensionless time:

$$\varepsilon_{ch} = \frac{T^*_{80} - T^*_{20}}{t^*_{80} - t^*_{20}}, \tag{10}$$

In this equation, the temperature is nondimensionalized by the following relation:

$$T^*_x = \frac{T_x}{T_h - T_c},$$

and the temperature T_x is calculated as:

$$T_x = T_c + x\%\cdot(T_h - T_c), \tag{11}$$

The time t_x denotes the moment at which the temperature of the fluid exiting the tank reaches the value T_x.

Dimensionless time t^*_x is a concept used to facilitate the comparison of storage tanks with different designs and mass flow rates. It is defined as the ratio of the operating time to the total replacement time, providing a normalized metric that allows for the evaluation of performance across varying systems. This concept is mathematically represented in the following equation:

$$t^*_x = \frac{t_x}{t_{total}}, \tag{12}$$

where t_{total} is the time of ideal discharging in a tank of volume V. In this study, the tank has a simple cylindrical shape, such that t_{total} can be simplified as:

$$t_{total} = \frac{V}{Q} = \frac{HS}{u_{in}S} = \frac{H}{u_{in}}, \tag{13}$$

It should be noted that u_{in} depends on the inlet geometry and area; therefore, this formulation provides an approximate basis for comparison among different inlet configurations rather than an absolute universal metric.

The *stratification number* is a parameter in the design and operation of thermal storage tanks, influencing system performance by quantifying the degree of thermal layering within the tank as shown in Figure 2. It measures the extent of thermal stratification, where hotter, less dense fluid resides at the top, and cooler, denser fluid settles at the bottom [25]. This stratification is essential for optimizing thermal storage and improving system efficiency. The stratification number is defined as:

$$Str(t) = \frac{\overline{\left(\frac{\partial T}{\partial z}\right)_t}}{\left(\frac{\partial T}{\partial z}\right)_{max}}, \tag{14}$$

where $\overline{\left(\frac{\partial T}{\partial z}\right)_t}$—average temperature gradients at different radial positions during specific time intervals. $\left(\frac{\partial T}{\partial z}\right)_{max}$—reference temperature gradient calculated using the maximum and minimum temperatures across the full height of the tank.

$$\overline{\left(\frac{\partial T}{\partial z}\right)_t} = \frac{1}{j-1}\left[\sum_{j=1}^{j-1}\left(\frac{T^t_{j+1} - T^t_j}{\Delta z}\right)\right], \tag{15}$$

$$\left(\frac{\partial T}{\partial z}\right)_{max} = \frac{T_{max} - T_{min}}{(j-1)\Delta z}, \tag{16}$$

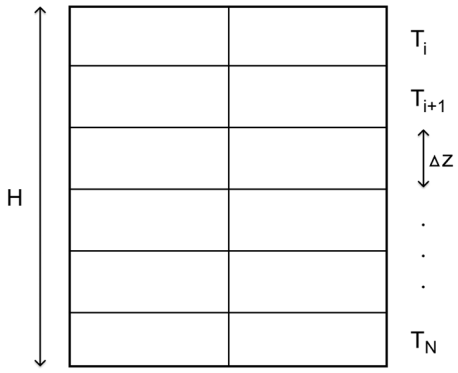


Figure 2. Tank layers for calculation of MIX and Str numbers. In our case: H = 3 m, Δz = 0.3, N = 11 (10 layers between 11 nodes.).

The degree of thermal mixing in the storage tank is quantified using the MIX number, defined according to a momentum-based formulation. The MIX number [25,26] is expressed as

$$\text{MIX} = \frac{M_{E,\text{stratified}} - M_{E,\text{exp}}}{M_{E,\text{stratified}} - M_{E,\text{fully-mixed}}} \tag{17}$$

The thermal momentum M_E is defined as the first moment of the thermal energy distribution along the vertical direction:

$$M_E = \sum_{i=1}^{N} y_i E_i \; with \; E_i = \rho_f c_p V_i T_i, \tag{18}$$

where T_i is the temperature of the i-th layer, V_i is the corresponding fluid volume, ρ_f is the fluid density, c_p is the specific heat capacity, and y_i is the vertical position of the layers measured from the bottom of the tank.

The experimental momentum $M_{E,\text{exp}}$ is computed directly from the measured temperature profiles. For the perfectly stratified reference state, the total thermal energy is assumed to be equal to the experimental energy,

$$E_{\text{stratified}} = E_{\text{exp}}, \tag{19}$$

and is represented using a two-zone model consisting of hot and cold regions at temperatures T_h and T_c, respectively. The volumes of the hot and cold regions are determined from the energy balance,

$$E_{\text{exp}} = V_{\text{hot}} \rho_f c_p T_h + V_{\text{cold}} \rho_f c_p T_c, V_T \tag{20}$$

The position of the thermocline is obtained from the cold volume and tank geometry, allowing the construction of an ideal two-zone temperature profile. The corresponding stratified momentum is then calculated as

$$M_{E,\text{stratified}} = \sum_{i=1}^{N} y_i \rho_f c_p V_i T_i^{\text{stratified}} \tag{21}$$

For the fully mixed reference state, the tank temperature is assumed to be spatially uniform and equal to the energy-weighted mean temperature,

$$T_{\text{fm}} = \frac{E_{\text{exp}}}{V_T \rho_f c_p}, \tag{22}$$

and the corresponding momentum is given by

$$M_{E,\text{fully}-\text{mixed}} = \sum_{i=1}^{N} y_i \rho_f c_p V_i T_{\text{fm}}. \quad (23)$$

A MIX number of 0 represents full stratification, where distinct temperature layers are maintained, minimizing entropy and maximizing exergy—ideal for thermal energy storage. A MIX number of 1 indicates complete mixing, with a uniform temperature throughout the tank, leading to a loss of thermal stratification and reduced storage efficiency. Thus, the MIX number quantifies the balance between thermal stratification and mixing, directly impacting system performance and energy efficiency [25,26].

2.3. Mesh Details

Mesh used for the various configurations. The computational analysis was performed using ANSYS Fluent 2024 R2. The simulations were conducted in a transient state to capture the dynamic nature of the heat storage process. Mesh refinement was performed iteratively to ensure accuracy and convergence. Post-processing tools in ANSYS Fluent were employed to visualize temperature distributions, velocity fields, and other relevant parameters. Python 3.9.7 (Python Software Foundation, Wilmington, DE, USA) was used for the analysis and processing of the results, enabling the extraction of data and the generation of detailed insights into the system's thermal and fluid dynamics.

Mesh details for the axisymmetric computations (open, groove and orifice inlets).

The 2D mesh used for the axisymmetric configurations is shown in Figure 3. Since the storage tank has a cylindrical geometry and symmetric inlet conditions, an axisymmetric approach was adopted, allowing a significant reduction in computational cost compared to full 3D simulations. The mesh parameters are summarized in Table 3.

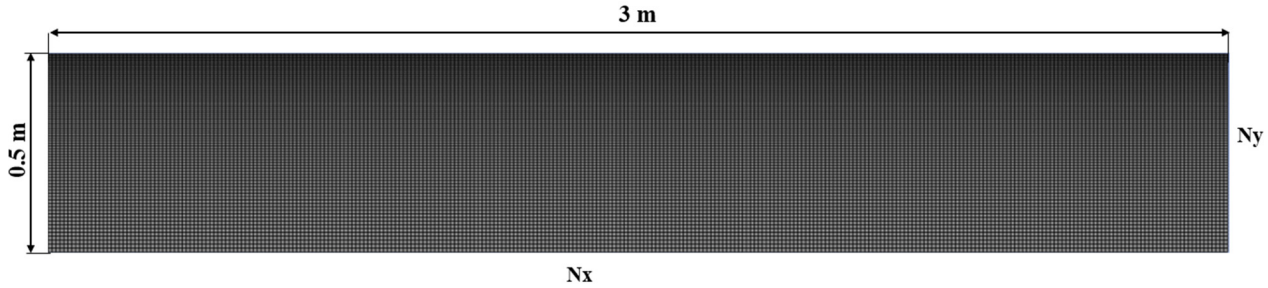


Figure 3. Mesh 1 for open, groove and orifice inlet.

Table 3. Mesh parameters used for the axisymmetric computations.

	Number of Divisions	Bias Factor
Inlet wall	80	3
Outlet wall	80	3
Tank wall	300 (hard)	-
axis	300 (hard)	-

For the shower and shower-groove inlet configurations, axisymmetry is not applicable and fully three-dimensional simulations were performed. The shower inlet case was discretized using a hybrid mesh with near-wall refinement and local refinement around the orifices. A similar strategy was applied to the shower-groove configuration, with additional refinement along the groove. Mesh statistics for these cases are reported in Table 4.

Table 4. Mesh parameters for the 3D simulations with symmetry.

Statistics	For Shower Inlet	For Shower Groove Inlet
Nodes	1,634,129	595,955
Elements	1,582,668	892,802

2.4. Model Validation: Comparison with Experimental Data, Mesh Independence, Time-Step Sensitivity, and Residual Convergence Analysis

The numerical model was validated by comparing the simulation results with independent experimental data reported by Zachar et al. [10]. In their experiments, a transparent vertical tank was used to observe thermocline development, where a tracer was introduced with the inlet flow entering from the bottom of the tank. To promote thermal stratification and suppress inlet-induced mixing, a thin flat plate was installed in the vicinity of the inlet (see Figure 4). Temperature evolution inside the tank was monitored using an array of 20 thermocouples distributed along the tank height, positioned between the central axis and the sidewall.

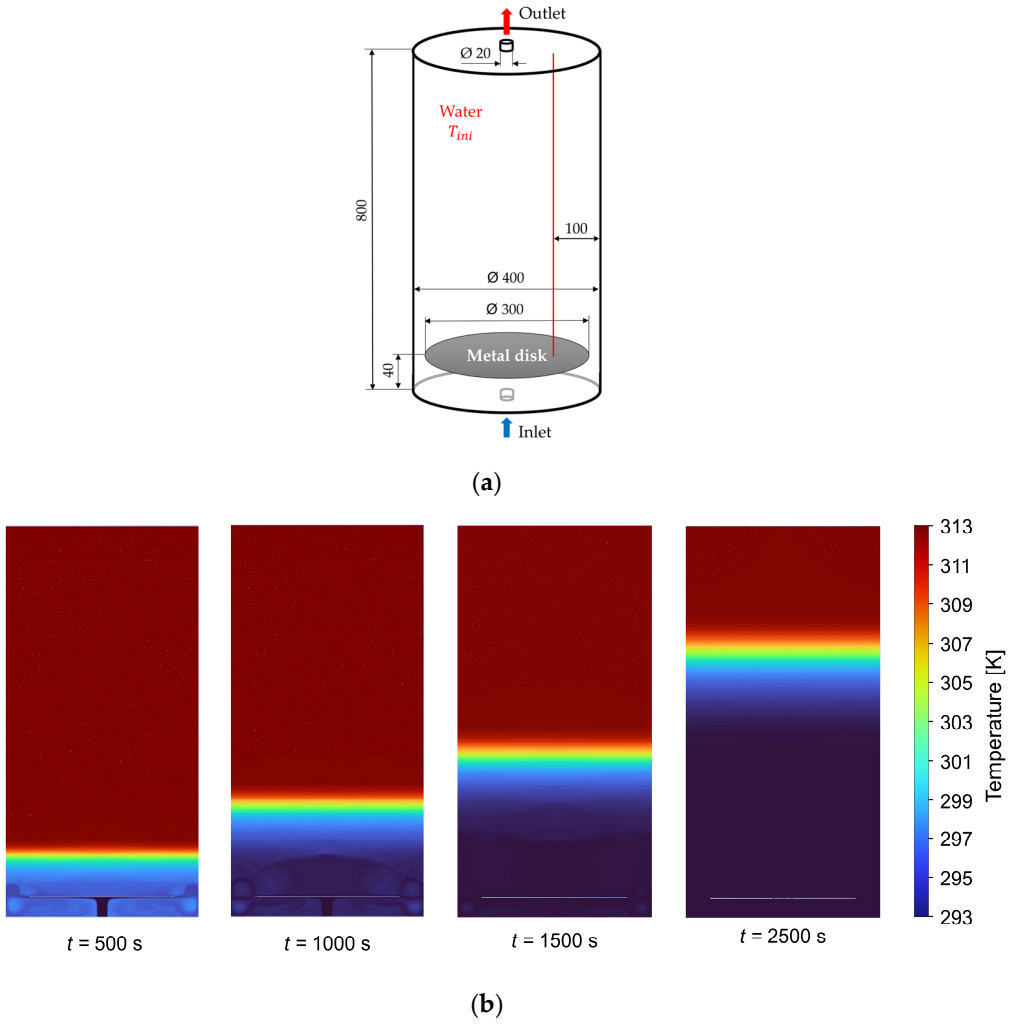


Figure 4. Configuration considered for validation purposes: (**a**) Sketch of the configuration considered in [10]; (**b**) Present 2D axisymmetric ANSYS Fluent results.

The experimental configuration considered a vertical cylindrical tank with a total height of 800 mm and an inner diameter of 400 mm, equipped with inlet and outlet nozzles each having a diameter of 20 mm. Temperature measurements were obtained using a vertical array of sensors located 100 mm from the tank sidewall. A thin circular plate with

a diameter of 300 mm was installed 40 mm above the tank bottom in the vicinity of the inlet. The function of this internal disk was to decrease the effective inlet velocity, forcing the heat transfer fluid to spread laterally around the plate and thereby promoting thermal stratification. At the start of the experiment, the water temperature inside the tank was 41 °C, while the inlet fluid entered at 20 °C with a volumetric flow rate of 1.6 L·min^{-1}, as reported in [10].

To facilitate comparison between the numerical predictions and the experimental measurements, a dimensionless temperature parameter T^* was defined as:

$$T^* = \frac{T - T_{in}}{T_{ini} - T_{in}} \tag{24}$$

The simulations were performed for a total duration of 2500 s, and the spatial distribution of the normalized temperature T^* was analyzed over time. Figure 4b illustrates the influence of introducing cold water at 20 °C on the evolution of the temperature field at selected time instants between 500 s and 2500 s. The results clearly demonstrate the progression of the discharge process and its effect on the development and deformation of thermal stratification layers. For validation purposes, the numerical results were subsequently compared with the corresponding experimental data.

Figure 5 presents a comparison between the axisymmetric numerical results obtained using ANSYS Fluent and the experimental data reported by Zachar et al. [10]. The comparison is performed at simulation times of 500 s, 1000 s, and 1500 s, corresponding to the temperature distributions shown in Figure 4b and the available experimental measurements. A quantitative evaluation of the mean temperature profiles shows good agreement between numerical and experimental results, with mean absolute errors (MAE) of 1.65%, 1.12%, and 2.58%, and corresponding root mean square errors (RMSE) of 5.01%, 2.03%, and 6.06% at 500 s, 1000 s, and 1500 s, respectively. These values indicate satisfactory predictive capability of the model over the investigated time range and no amplification of the errors over the simulation time.

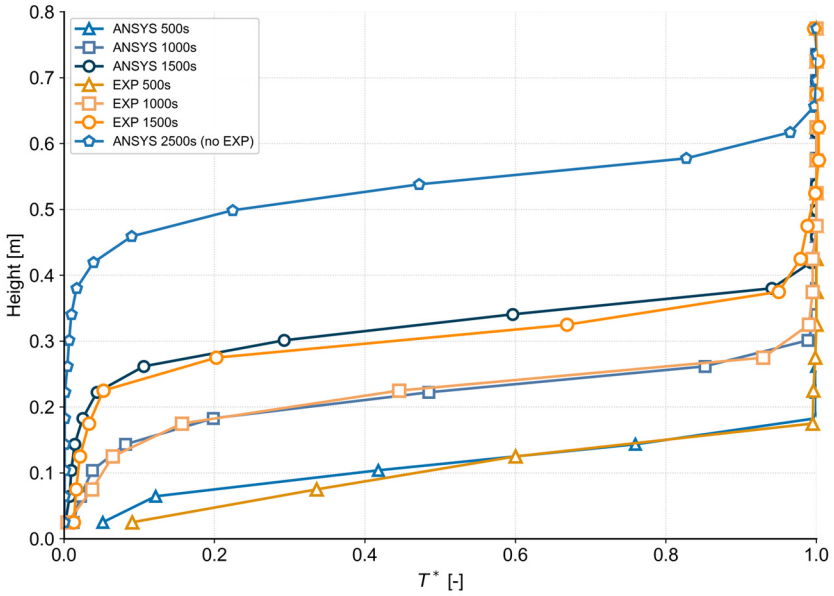


Figure 5. Comparison of the dimensionless temperature profiles along the tank height at t = 500 s, 1000 s, 1500 s, and the numerical profile at 2500 s.

Although the experiments reported by Zachar et al. [10] were conducted up to 2500 s, the published study does not provide temperature profile data at this time instant. For completeness and to illustrate the temporal evolution of the thermocline, the numerical

temperature profile at 2500 s is also presented in Figure 5; however, no experimental comparison is available for this time step.

Based on the obtained results, the axisymmetric numerical framework developed in ANSYS Fluent is shown to reliably capture the dominant physical processes governing heat transfer and thermal stratification in a sensible thermal energy storage tank. The validated model can therefore be applied with confidence to parametric studies involving different inlet and outlet configurations, as well as to simulations with alternative working fluids.

Subsequently, the influence of grid resolution, time-step size, and residual convergence criteria on the accuracy of the numerical solution is assessed. All comparisons were conducted using the open-inlet configuration (with mass flow rate Q_1). The study investigates how varying these parameters affects the precision of the problem's solution, highlighting the trade-off between accuracy and computational cost (see Table 5). It is shown that decreasing the grid size and time step improves accuracy, but also leads to increased computational time and resource requirements. The results obtained for different values of these parameters are analyzed to assess their influence on the accuracy and stability of the numerical solution. In Table 5, ε_u represents the convergence criterion for the momentum (velocity) equations, while ε_T denotes the convergence criterion for the energy equation expressed in terms of temperature.

Table 5. Accuracy check.

№	Mesh	Residuals		Δt
1	M_2	$\varepsilon_u = 10^{-3}$	$\varepsilon_T = 10^{-6}$	5
2	M_1	$\varepsilon_u = 10^{-6}$	$\varepsilon_T = 10^{-6}$	5
3	M_1	$\varepsilon_u = 10^{-3}$	$\varepsilon_T = 10^{-6}$	2.5

An analysis was performed to evaluate the adequacy of the computational grid and to verify the appropriateness of the selected time-step size and residual convergence criteria. This analysis included a thorough evaluation of grid resolution, time step stability, and residual convergence to ensure the simulation's accuracy and physical representativeness. To begin, two types of meshes (M_1 and M_2) were compared: M_2 is the finer mesh, with $\sqrt{2}$ times as many divisions in each direction as M_1.

Mesh checking. In this case, the orange line represents the results for mesh M_2, while the blue line corresponds to mesh M_1 as shown Figure 6. These lines illustrate the temperature variation over time at the inlet.

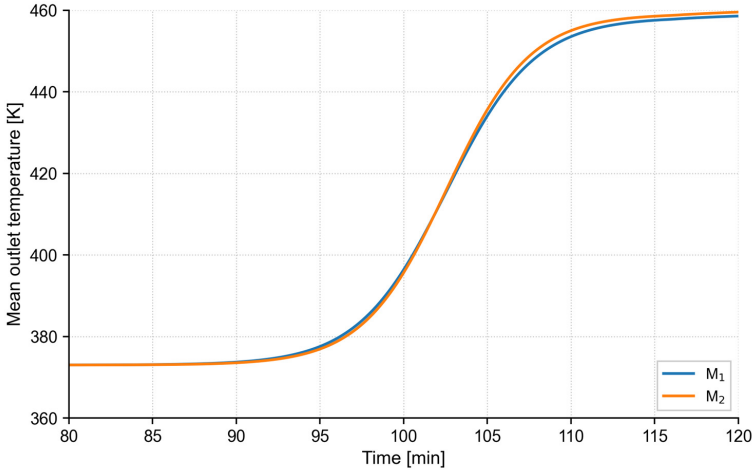


Figure 6. Mesh independence check: comparison of mean outlet temperature for two meshes (M_1—blue, M_2—orange) using Δt = 5 s, $\varepsilon_u = 10^{-3}$, and $\varepsilon_T = 10^{-6}$ for the open inlet configuration.

The outlet temperature exhibited minimal variation, indicating that the use of a finer mesh did not significantly alter the results. This observation suggests that the computational effort required for finer mesh, which entails a longer compilation time, may not be justified. Our first mesh M_1 is sufficiently accurate for further calculations.

Residuals were used solely as indicators of solver convergence. They indicate how well the discretized continuity, momentum, and energy equations are satisfied at each iteration. Convergence was declared when normalized residuals fell below $\varepsilon_u = 10^{-3}$ and $\varepsilon_T = 10^{-6}$. A sensitivity check on mesh M_1, in which the residual target ε_u was reduced from 10^{-3} to 10^{-6} while ε_T was kept unchanged, increased the iteration count but did not modify the solution within the stated precision, as shown in Figure 7 ($\varepsilon_u = 10^{-3}$ (blue), $\varepsilon_u = 10^{-6}$ (orange)); therefore, $\varepsilon_u = 10^{-3}$ was retained for the baseline calculations.

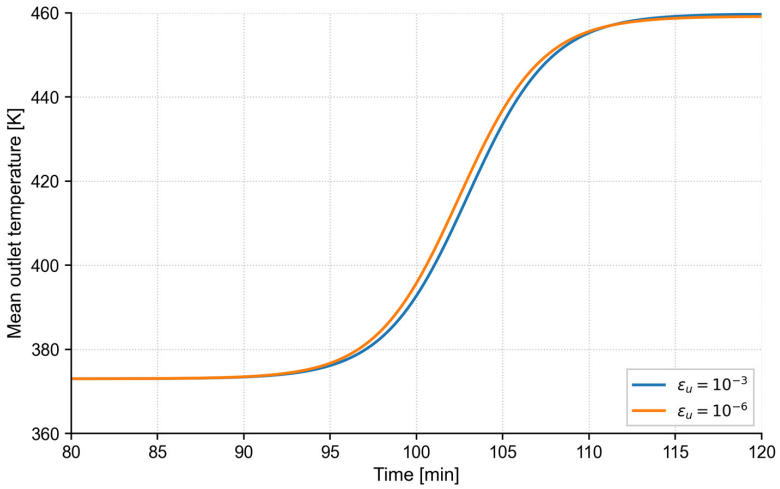


Figure 7. Residual convergence check: comparison of mean outlet temperature for mesh M_1 using two residual criteria ($\varepsilon_u = 10^{-3}$, and $\varepsilon_T = 10^{-6}$) at $\Delta t = 5$ s.

The time step was halved from $\Delta t = 5$ s (blue) to 2.5 s (orange). Figure 8 shows the outlet temperature as a function of time for both time steps; the curves are nearly indistinguishable over the entire interval. Reducing Δt increases computational cost but does not materially change the solution within the stated precision. Accordingly, $\Delta t = 5$ s was used in subsequent calculations.

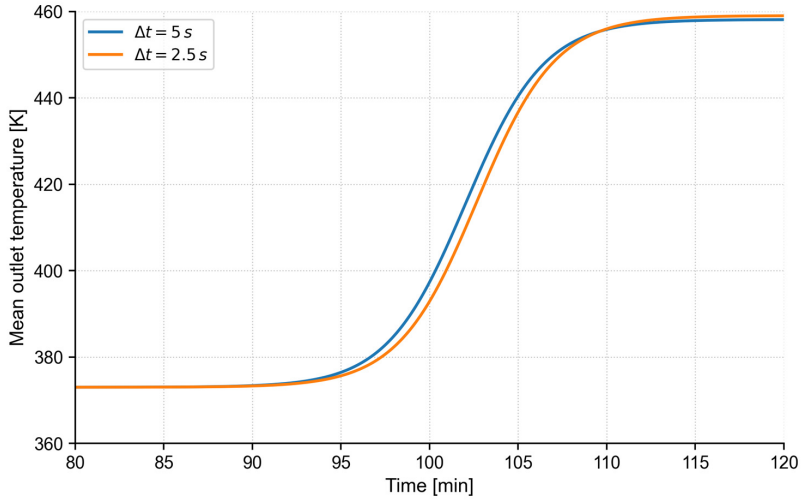


Figure 8. Time-step sensitivity analysis: comparison of mean outlet temperature for two time steps ($\Delta t = 5$ s and $\Delta t = 2.5$ s) using mesh M_1, $\varepsilon_u = 10^{-3}$, and $\varepsilon_T = 10^{-6}$ for the open inlet configuration.

2.5. Research Methods

To obtain an accurate and stable solution of the governing equations, appropriate numerical methods and discretization schemes available in ANSYS Fluent 2024 R2 were selected. The choice of these methods has a significant influence on the convergence behaviour, numerical stability, and overall accuracy of the simulations, particularly for transient nonlinear processes and non-uniform computational grids. In the present study, the following schemes were employed:

The Fractional Step method was applied to simplify the solution procedure by dividing the calculation into two stages: first solving for the velocity field and then adjusting for the pressure. For gradient evaluation, the Least Squares Cell Based method was adopted, as it provides higher accuracy on irregular meshes. To accurately model convection in the momentum and energy transport equations, the second-order QUICK scheme was used. Pressure correction was carried out using the PRESTO! Scheme, particularly suitable for flows with strong pressure variations. Finally, for the transient formulation, a Bounded Second Order Implicit scheme was employed, ensuring higher accuracy for time-dependent simulations by applying a more advanced second-order approach to account for variations over time.

The NITA (Non-Iterative Time Advancement) method in ANSYS Fluent was also employed to accelerate the solution of transient fluid dynamics problems. This method eliminates the need for multiple inner iterations at each time step, significantly reducing the number of computational steps and, consequently, the overall computational cost. The NITA method enhances numerical stability, particularly in cases where traditional methods struggle to converge due to strong oscillations or abrupt parameter changes over time. It solves the linear equations in a single step using predicted and corrected values of the variables, thus speeding up the simulation. This approach is especially effective for modelling fast processes requiring small time steps, such as acoustic phenomena, turbulent bursts, and rapid pressure changes.

3. Results and Discussion

This section presents the results of a 2D-3D CFD analysis of a hot working fluid storage tank. The analysis focuses on thermal stratification and fluid dynamics during the charging process, with varying inlet configurations and mass flow rates. As stated above, only the charging process of the thermal storage tank is considered in the present study. Initially, the thermal oil inside the tank is uniformly at a temperature of 373 K, while the hot working fluid enters the tank from the top at an inlet temperature of 523 K. The storage tank is considered fully charged when the temperature at the bottom of the tank reaches 80% of the inlet working-fluid temperature, as defined by Equation (11). For the first configuration with an open inlet, complete charging of the storage tank required approximately 120 min, as determined from the temporal evolution of the temperature field. For consistency and comparative purposes, temperature contours for all other inlet configurations were therefore visualized and analyzed over the same charging duration of 120 min. The results include temperature distributions, flow patterns, and the impact of different inlet configurations on thermal storage efficiency. Performance indicators for five inlet configurations are discussed, and conclusions are drawn based on the simulation results.

Figure 9 presents the instantaneous temperature contours (in K) for the different inlet configurations at selected charging times. The results reveal markedly different flow and thermal patterns within the storage tank, which are governed primarily by inlet-induced momentum transport and viscous shear, as described by the incompressible Navier–Stokes equations coupled with the energy equation. In the absence of buoyancy forces, thermal

stratification and mixing are controlled by the balance between advective heat transport, viscous diffusion, and inlet jet dynamics.

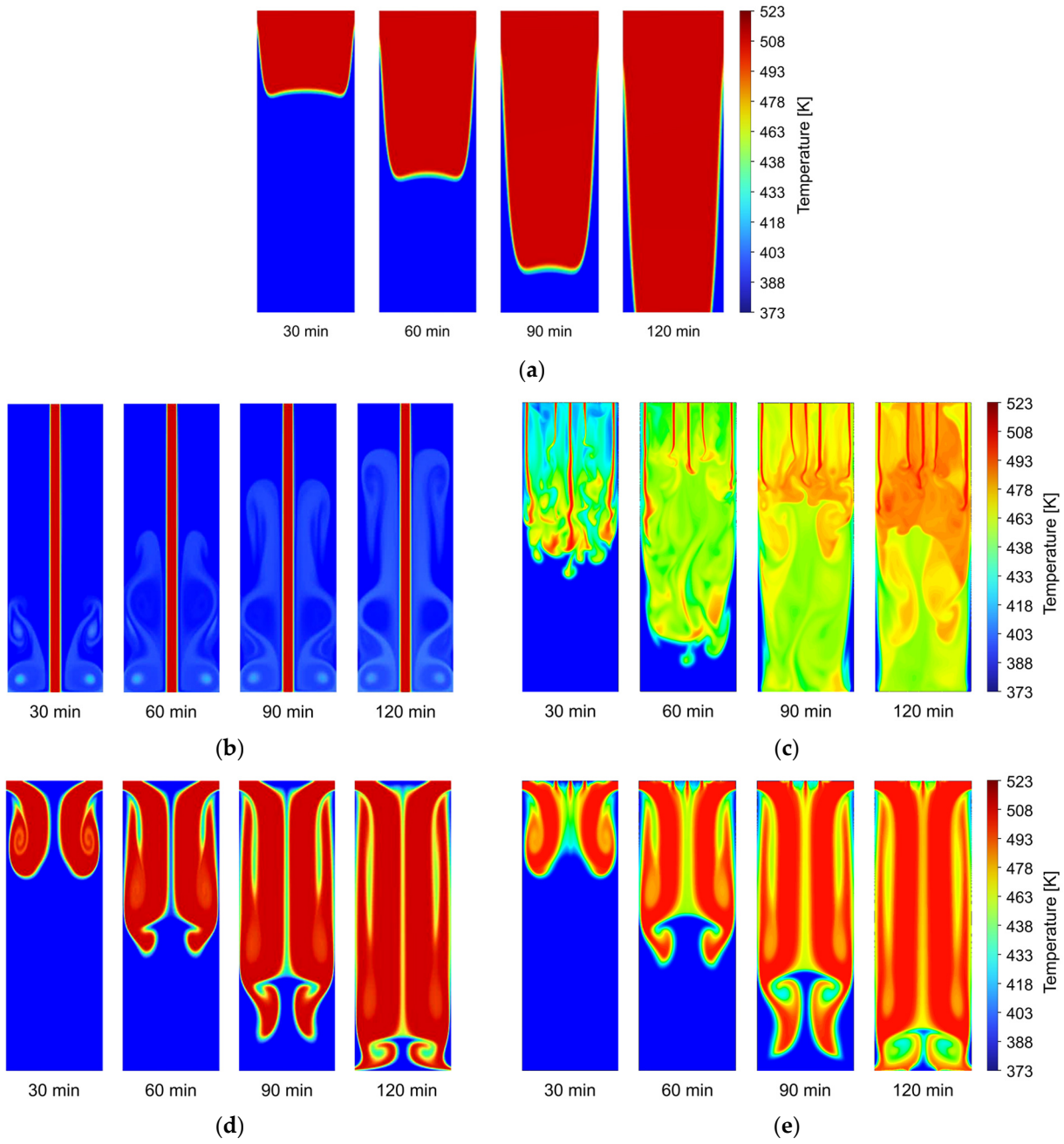


Figure 9. Temperature contours of the heat transfer fluid at different times for the four inlet configurations: (**a**) open inlet; (**b**) orifice inlet; (**c**) shower inlet; (**d**) groove inlet; (**e**) shower-groove inlet, all at flow rate Q_1.

For the shower inlet configuration (Figure 9), the inflow is distributed through multiple small orifices, generating several high-velocity jets that penetrate into the colder fluid region. These jets interact and merge, producing strong shear layers and large-scale recirculation zones. As a result, vortical structures develop throughout the tank, enhancing momentum exchange and advective heat transport in the vertical direction. This leads to intensive mixing of the working fluid and a nearly uniform temperature field, thereby suppressing the formation of stable thermal layers. Consequently, despite effective heat penetration, this configuration is ineffective in maintaining thermal stratification under forced-convection-dominated conditions.

In contrast, the groove and shower-groove inlet configurations (Figure 9d,e) promote a more controlled flow development. The inlet geometry reduces the effective jet momentum and redistributes the incoming flow along the tank cross-section, weakening vertical penetration and limiting shear-induced instabilities. As a result, advective transport is confined to a relatively thin transition region, while thermal diffusion governs heat transfer across the thermocline. This flow regime allows distinct temperature layers to persist over time, leading to improved thermal stratification and more efficient heat accumulation within the tank.

The orifice inlet configuration (Figure 9) exhibits irregular temperature distributions and weak stratification. The concentrated inlet jet induces localized high-velocity regions and asymmetric recirculation, which disrupt the formation of coherent thermal layers. Although heat is introduced into the tank, the dominance of jet-induced advection over diffusive transport prevents the establishment of a stable thermocline, resulting in poor stratification stability and reduced storage effectiveness.

The open inlet configuration (Figure 9a) represents an idealized reference case that is not feasible in HTF storage systems and is therefore included solely for comparative purposes. Due to the absence of inlet flow control, this configuration promotes strong vertical advection and extensive mixing, and no further analysis is pursued for this case.

All temperature fields in Figure 9 are shown at regular time intervals of 30 min up to a total charging duration of 120 min. This time horizon was selected based on the observation that, under ideal forced-convection conditions, a tank of the present dimensions reaches the target thermal accumulation within approximately 2 h. The temporal evolution of the temperature contours provides insight into the development of flow structures, the progression of heat penetration, and the degradation or preservation of thermal stratification during the charging process.

Figure 10 summarizes the performance indicators obtained for the different inlet configurations at the mass flow rate Q_1. The observed trends directly reflect the inlet-induced flow structures and the balance between advective heat transport and mixing mechanisms discussed previously.

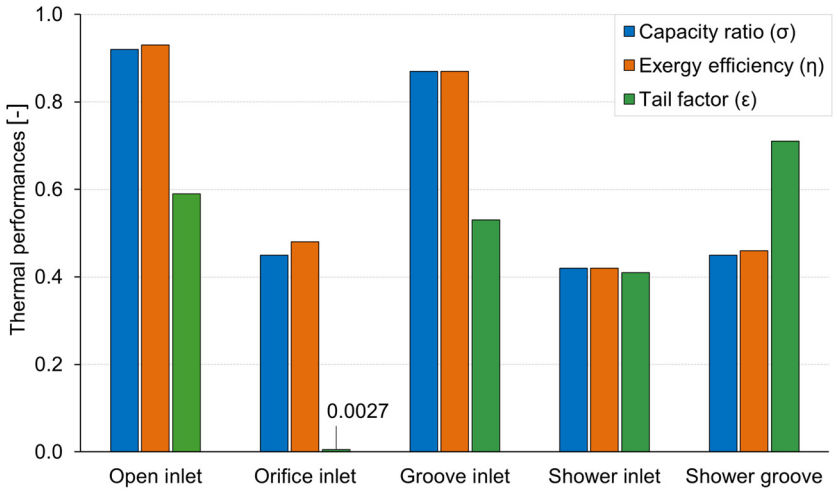


Figure 10. Thermal performances of different configurations at same mass flow rate Q_1.

The open and groove inlet configurations exhibit the highest values of both capacity ratio and exergy efficiency, approaching 0.9. From a physical standpoint, this behavior is associated with strong advective heat transport driven by inlet momentum, which allows rapid energy transfer into the tank volume. In the case of the groove inlet, however, the inlet geometry partially redistributes the incoming momentum along the tank cross-section,

reducing excessive jet penetration and limiting shear-induced mixing. As a result, high energy utilization is achieved while preserving a relatively stable thermal layering.

Although the open inlet also demonstrates high energetic and exergetic performance, this configuration is not suitable for practical applications, as the absence of flow control leads to intense vertical advection and large-scale recirculation. These effects, governed by the convective terms of the Navier–Stokes equations, promote strong mixing and progressively degrade thermal stratification, as reflected by the comparatively lower tail factor.

The orifice and shower inlet configurations show moderate performance, with capacity ratio and exergy efficiency values around 0.4–0.5. In these cases, concentrated inlet jets generate localized high-velocity regions, which enhance viscous dissipation and momentum exchange throughout the tank. The dominance of jet-induced advection over diffusive heat transport prevents the formation of a sharp thermocline, leading to reduced useful energy storage despite continuous heat input.

The shower-groove inlet exhibits a distinct behavior. While its capacity ratio and exergy efficiency remain moderate, its tail factor reaches the highest value (~0.71) among the investigated configurations. This indicates improved stratification quality and reduced thermal mixing. Physically, this performance results from the combined action of momentum dissipation through multiple orifices and lateral flow redistribution along the groove, which suppresses large-scale vortical structures and confines advective transport to a limited region near the inlet. Consequently, thermal diffusion dominates across the thermocline, allowing temperature gradients to be maintained over longer periods.

Overall, the groove inlet emerges as the most balanced and optimal configuration, providing high capacity ratio and exergy efficiency while maintaining acceptable stratification stability. The shower-groove inlet may be preferable in applications where preserving stratification is prioritized over maximum energy throughput. These results confirm that inlet geometry plays a decisive role in controlling forced-convection-driven mixing and, therefore, should be selected based on the targeted compromise between energy efficiency, exergy performance, and stratification stability.

3.1. Effect of Mass Flow Rate and Inlet Configuration on Temperature Distribution

This section examines the influence of mass flow rate on the thermal and energetic performance of the storage tank. Numerical simulations were conducted at the reference flow rate $Q_1 = 3.0 \times 10^{-4}$ m^3 s^{-1}, as well as at two reduced flow rates, $Q_2 = Q_1/2$ and $Q_3 = Q_1/3$. Temperature contours corresponding to the groove, shower, and shower-groove inlet configurations are presented in Figure 11. These results allow a systematic assessment of how variations in inlet momentum affect thermal stratification and heat storage efficiency for each configuration.

As illustrated in Figure 11, the mass flow rate exerts a strong influence on the development and preservation of thermal stratification. At higher flow rates, the increased inlet velocity enhances the advective terms in the momentum equations, leading to stronger jet penetration [27], elevated shear stresses, and the formation of large-scale recirculation zones. These flow structures intensify momentum exchange across the tank height, promoting vigorous mixing and accelerating the homogenization of the temperature field. Consequently, vertical temperature gradients are progressively weakened, resulting in a reduction in thermal stratification despite efficient heat transport into the tank.

In contrast, at lower mass flow rates, the reduced inlet momentum limits jet penetration and suppresses shear-induced instabilities. Under these conditions, advective transport is confined to a narrower region near the inlet, while viscous dissipation and thermal diffusion dominate the heat transfer process across the thermocline. This balance allows temperature differences between the upper and lower regions of the tank to persist for

longer durations, leading to the formation of more stable and well-defined thermal layers. As a result, stratification quality improves, although the overall rate of energy accumulation decreases due to the reduced convective heat flux.

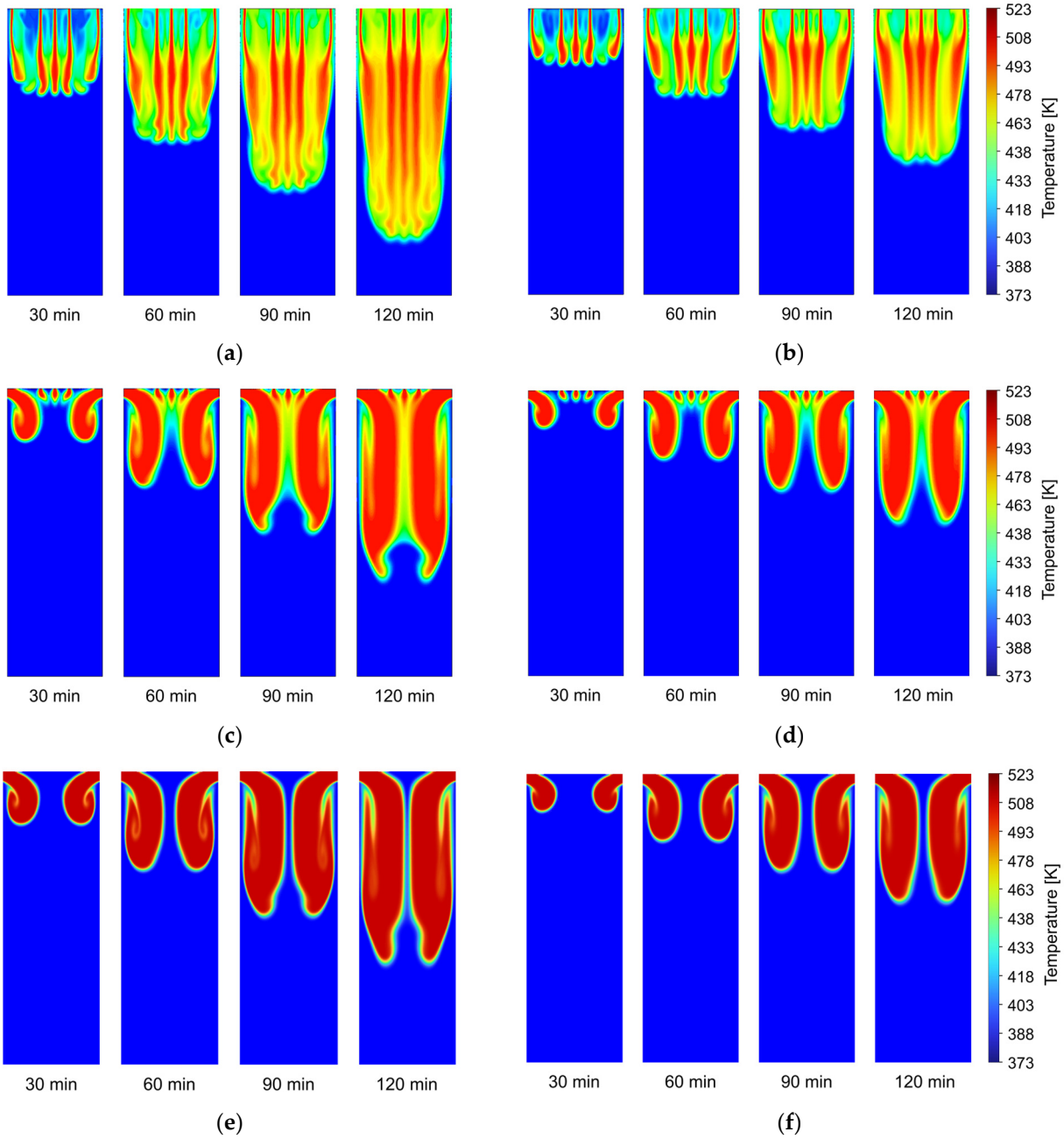


Figure 11. Temporal evolution of the heat transfer fluid temperature field at 30, 60, 90, and 120 min for three inlet configurations at two different mass flow rates: (**a**) shower inlet at Q_2; (**b**) shower inlet at Q_3; (**c**) shower-groove inlet at Q_2; (**d**) shower-groove inlet at Q_3; (**e**) groove inlet at Q_2 (**f**) groove inlet at Q_3.

The inverse relationship between mass flow rate and stratification intensity observed in Figure 11 is therefore a direct consequence of forced-convection dynamics. Increasing the mass flow rate enhances heat transfer efficiency by accelerating energy delivery but simultaneously degrades stratification through momentum-driven mixing. Conversely, decreasing the mass flow rate weakens mixing, preserves thermal layering, and improves stratification stability, at the expense of longer charging times. These trends are consistent

across all inlet configurations, although their magnitude depends on the ability of each inlet geometry to dissipate or redistribute inlet momentum.

Overall, the results highlight that optimal thermal energy storage performance requires a compromise between convective heat transfer efficiency and stratification preservation. This compromise can be achieved by appropriately selecting both the inlet configuration and the operating mass flow rate, depending on whether rapid charging or long-term thermal stratification is prioritized.

3.2. MIX and Stratification Numbers for Different Inlet Configurations and Mass Flow Rates

Figures 12–14 present the temporal evolution of the MIX number and the stratification number for the shower, groove, and shower-groove inlet configurations under three different mass flow rates (Q_1, Q_2, and Q_3). These two indicators provide complementary information: the MIX number quantifies the global degree of energy redistribution within the tank, whereas the stratification number characterizes the strength of the vertical temperature gradient and, therefore, the quality of thermal layering.

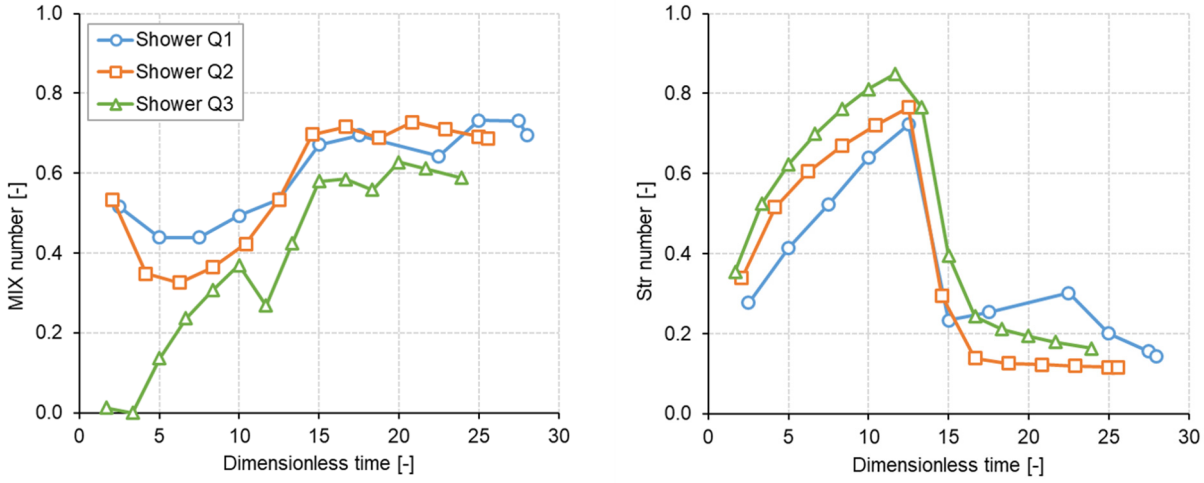


Figure 12. Performance indicators for the shower inlet configuration at three mass flow rates (Q_1—blue, Q_2—orange, Q_3—green): (**a**) MIX number; (**b**) stratification number.

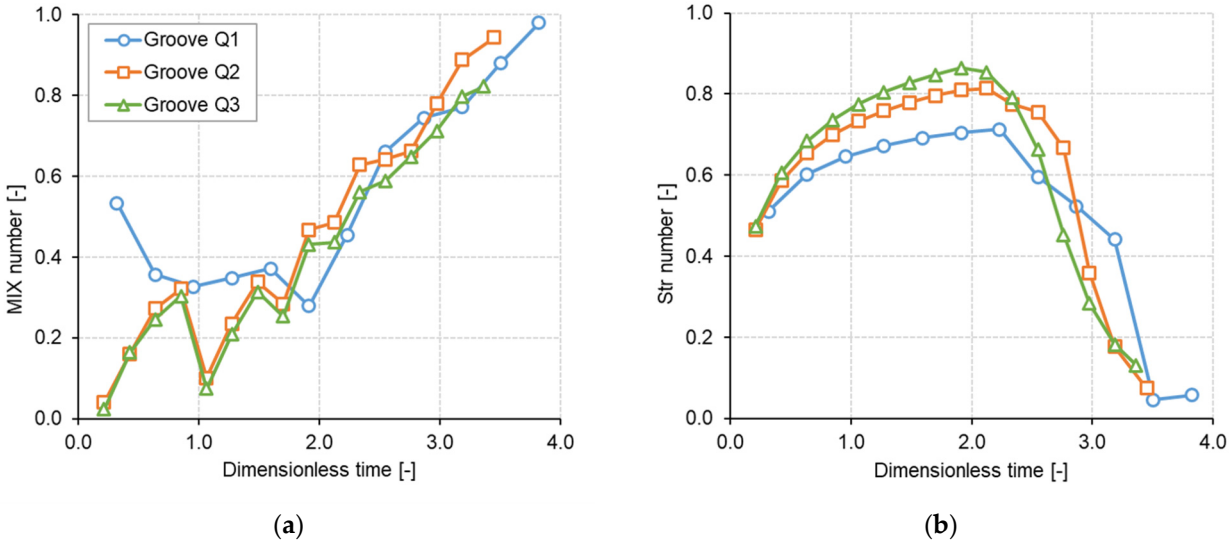


Figure 13. Performance indicators for the groove inlet configuration at three mass flow rates (Q_1—blue, Q_2—orange, Q_3—green): (**a**) MIX number; (**b**) stratification number.

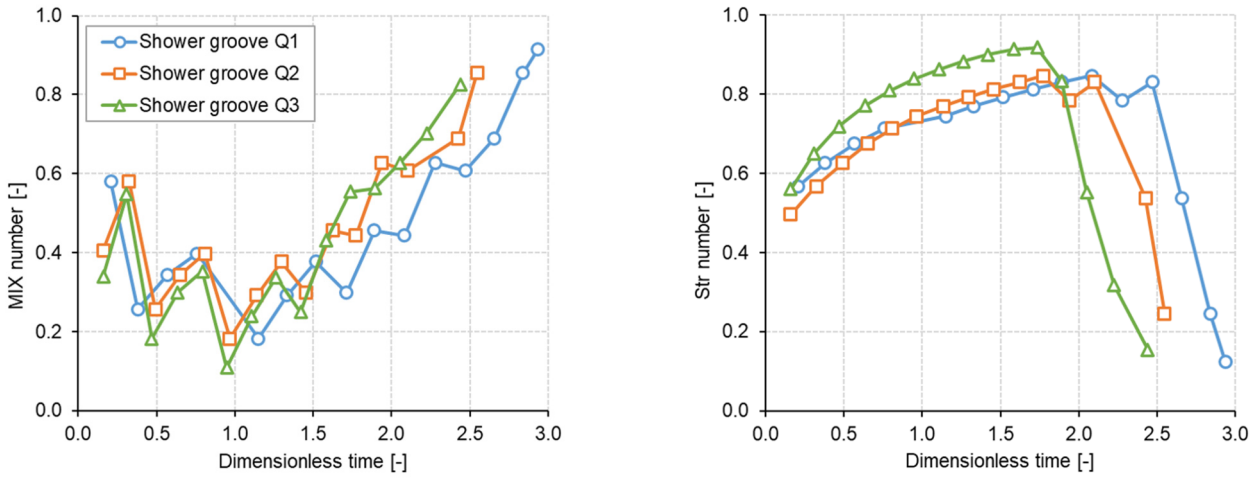


Figure 14. Performance indicators for the shower groove inlet configuration at three mass flow rates (Q_1—blue, Q_2—orange, Q_3—green): (**a**) MIX number; (**b**) stratification number.

For the shower inlet configuration (Figure 12), the MIX number exhibits a gradual increase with time for all mass flow rates, indicating progressive redistribution of thermal energy throughout the tank during the charging process. At early times, the MIX curves for Q_1, Q_2, and Q_3 remain close to each other, reflecting similar initial energy penetration patterns. As charging proceeds, slight divergence is observed; however, all cases approach comparable MIX values at later times. This behavior suggests that, for the shower inlet, the overall degree of mixing is primarily governed by the inlet-induced jet structure rather than by moderate variations in mass flow rate.

The stratification number shows a clear dependence on the flow rate. At the highest flow rate (Q_1), the stratification number remains consistently lower, indicating stronger momentum-driven mixing and a weaker vertical temperature gradient. For reduced flow rates (Q_2 and Q_3), higher initial stratification levels are achieved, as the lower inlet momentum limits jet penetration and reduces shear-induced mixing. Nevertheless, as charging continues, the stratification number decreases in all cases, demonstrating a gradual degradation of thermal layering due to cumulative advective transport and thermal diffusion. This confirms that, for the shower inlet, strong mixing dominates the flow dynamics, ultimately limiting long-term stratification regardless of the mass flow rate.

In the groove inlet configuration (Figure 13), both performance indicators exhibit more pronounced sensitivity to the mass flow rate. The MIX number increases more slowly compared to the shower inlet, particularly for the lowest flow rate (Q_3), indicating reduced global mixing and a more confined redistribution of thermal energy. This behavior is consistent with the groove geometry, which redistributes inlet momentum laterally and suppresses deep jet penetration.

The stratification number reaches significantly higher peak values than in the shower inlet case, especially for Q_2 and Q_3. This reflects the formation of a well-defined thermocline and the preservation of strong vertical temperature gradients over an extended period. At higher flow rates, stratification initially increases due to efficient energy delivery but subsequently declines as enhanced advection gradually erodes the thermal layers. At lower flow rates, the stratification number remains higher for longer times, confirming that reduced inlet momentum promotes stable stratification by limiting interlayer mixing. Overall, the groove inlet demonstrates an effective balance between heat accumulation and stratification preservation, particularly under moderate and low flow conditions.

For the shower-groove inlet configuration (Figure 14), the MIX number shows intermediate behavior between the shower and groove cases. Although mixing increases with time for all flow rates, the rate of increase is slower than for the shower inlet, indicating improved control of energy redistribution. Differences between Q_1, Q_2, and Q_3 are more apparent, with lower flow rates consistently yielding smaller MIX values, corresponding to reduced mixing intensity.

The stratification number attains the highest values among all configurations, particularly for Q_2 and Q_3. This confirms that the combined action of flow distribution through multiple openings and momentum dissipation along the groove effectively suppresses large-scale vortical structures. As a result, advective transport is confined near the inlet region, while thermal diffusion governs heat transfer across the thermocline. Although stratification eventually decreases at later times for all flow rates, the shower-groove configuration maintains superior stratification quality over the entire charging process.

Across all configurations, the MIX number exhibits a general increasing trend with time, reflecting the inevitable redistribution of thermal energy during charging. However, its relatively weak sensitivity to mass flow rate, particularly for the shower inlet, indicates that inlet geometry plays a dominant role in controlling global mixing behavior. In contrast, the stratification number is strongly affected by both inlet configuration and flow rate, making it a more sensitive indicator of thermal layering quality.

The results clearly demonstrate that lower mass flow rates favor stratification preservation, as reduced inlet momentum weakens shear-induced mixing and allows vertical temperature gradients to persist. Conversely, higher flow rates enhance heat transfer efficiency at the expense of stratification stability. Among the investigated designs, the groove and shower-groove inlets provide the most favorable compromise between energy accumulation and stratification maintenance, with the shower-groove configuration exhibiting the highest resistance to stratification degradation over time.

3.3. Performance Comparison of Inlet Configurations at Different Mass Flow Rates

The performance indicators obtained for the different inlet configurations and flow rates reveal clear trends in the thermal and exergy behavior of the storage tank. Tables 6–8 compare the performance indicators at different flow rates for the various inlet configurations. The groove inlet configuration exhibits the best energy efficiency, especially at high flow rates. This configuration outperforms both the shower inlet and shower groove inlet across all tested flow rates. The shower inlet and shower groove inlet configurations show moderate to low efficiency, with little variation across different flow rates. Therefore, for optimal energy efficiency, the groove inlet is the preferable configuration, particularly when operating at higher flow rates.

Table 6. Performance indicators of the shower inlet configuration at different flow rates.

Shower Inlet Flow Rate	Capacity Ratio (σ)	Exergy Efficiency (η)	Tail Factor (ε)
Q_1	0.42	0.42	0.41
Q_2	0.39	0.40	0.51
Q_3	0.39	0.40	0.61

Table 7. Performance indicators of the groove inlet configuration at different flow rates.

Groove Inlet Flow Rate	Capacity Ratio (σ)	Exergy Efficiency (η)	Tail Factor (ε)
Q_1	0.87	0.87	0.53
Q_2	0.83	0.83	0.88
Q_3	0.82	0.83	0.69

Table 8. Performance indicators of the shower groove inlet configuration at different flow rates.

Shower Groove Inlet Flow Rate	Capacity Ratio (σ)	Exergy Efficiency (η)	Tail Factor (ε)
Q_1	0.45	0.46	0.71
Q_2	0.41	0.41	1.05
Q_3	0.40	0.40	1.13

The data suggests that the groove inlet and shower groove inlet exhibit a higher sensitivity to changes in flow rates compared to the shower inlet. Specifically, the tail factor for the groove inlet shows a marked increase at flow rate Q_2, while the shower groove inlet demonstrates a steady increase in tail factor across all flow rates, peaking at Q_3. This indicates that the groove inlet and shower groove inlet configurations might be more effective or efficient in managing fluid flow at higher rates compared to the shower inlet. Further analysis and testing could provide insights into optimizing these inlets for specific applications based on their flow rate responses.

For the shower inlet configuration (Table 6), the highest capacity ratio and exergy efficiency are obtained at the maximum mass flow rate Q_1, with values of 0.42. As the mass flow rate decreases to Q_2 and Q_3, both indicators slightly decrease to approximately 0.40, indicating a reduction in heat transfer effectiveness due to weaker convective transport. Meanwhile, the tail factor increases from 0.41 at Q_1 to 0.61 at Q_3, suggesting enhanced thermal stratification at lower flow rates. Nevertheless, even at reduced flow rates, the shower inlet exhibits relatively limited stratification capability compared to the other configurations, owing to stronger mixing induced by the inlet geometry.

Decrease in both energy and exergy efficiencies with a lower flow rate is primarily due to reduced heat transfer efficiency, increased irreversibility, and deviation from the optimal operating point of the system. Understanding these dependencies can help in optimizing the operation to maintain high efficiencies.

For the groove inlet configuration (Table 7), consistently higher performance is observed over the entire range of operating conditions. At Q_1, both the capacity ratio and exergy efficiency reach their maximum values of 0.87, indicating highly efficient energy utilization. This condition is accompanied by a relatively low tail factor (0.53), reflecting enhanced mixing at high inlet momentum. When the flow rate is reduced to Q_2, the capacity ratio and exergy efficiency slightly decrease to 0.83, while the tail factor increases markedly to 0.88, indicating improved thermal stratification due to reduced momentum penetration. At Q_3, the system maintains a favorable balance between energy efficiency and stratification, with a capacity ratio of 0.82 and a tail factor of 0.69. These results demonstrate that the groove inlet provides an effective compromise between thermal performance and stratification preservation.

For the shower-groove inlet configuration (Table 8), the capacity ratio and exergy efficiency are lower than those of the groove inlet but higher than those of the shower inlet. Specifically, the capacity ratio decreases from 0.45 at Q_1 to 0.40 at Q_3, while the tail factor increases from 0.71 to 1.13. The relatively high tail factor values indicate strong preservation of thermal stratification, particularly at low flow rates. This behavior can be attributed to the combined effect of flow redistribution and momentum dissipation provided by the shower-groove geometry, which suppresses large-scale mixing and promotes stable thermal layering.

The results reveal a clear trade-off between energy efficiency and stratification quality. Higher mass flow rates enhance heat transfer and increase both capacity ratio and exergy efficiency, but simultaneously intensify mixing and weaken stratification. Conversely, lower flow rates favor stratification preservation at the expense of reduced energetic performance. Among the investigated configurations, the groove inlet provides the most balanced overall

performance, while the shower-groove inlet offers the highest resistance to stratification degradation, making it particularly suitable for applications where thermal layering is of primary importance.

4. Conclusions

This study numerically investigated the effects of inlet configuration and mass flow rate on the thermal, energetic, and stratification performance of a sensible thermal energy storage tank during the charging process.

The results show that inlet geometry is the primary factor controlling mixing and stratification, while the mass flow rate governs the trade-off between charging efficiency and thermal layering. Among all configurations, the groove inlet provided the best overall performance, achieving a maximum capacity ratio and exergy efficiency of 0.87 at the highest flow rate. When the flow rate was reduced, the groove inlet preserved high efficiency (capacity ratio $\approx$ 0.82–0.83) while significantly improving stratification, with the tail factor increasing up to 0.88, indicating a favorable balance between energy storage and stratification stability.

The shower-groove inlet exhibited the strongest thermal stratification, particularly at low flow rates, reaching a maximum stratification number of 1.13 and tail factor values above 1.0. However, this enhanced stratification was accompanied by lower energetic performance, with capacity ratio and exergy efficiency limited to approximately 0.40–0.45. In contrast, the shower and orifice inlets showed stronger mixing, weaker stratification, and lower overall efficiency across all operating conditions.

The results confirm a clear efficiency-stratification trade-off. The groove inlet is recommended for applications prioritizing high energy and exergy efficiency with acceptable stratification, while the shower-groove inlet is better suited for systems where long-term thermal stratification is the primary design objective.

Future studies will investigate the influence of optimized inlet configurations in TES systems containing packed-bed or PCM elements to assess their impact on flow distribution and storage performance.

Author Contributions: Conceptualization, A.K. (Abdelhamid Kheiri); methodology, A.K. (Abdelhamid Kheiri) and O.B.; software, A.K. (Aiym Kereikulova); validation, A.K. (Aiym Kereikulova), O.B., and Y.B.; formal analysis, A.K. (Aiym Kereikulova) and Y.Y.; investigation, A.K. (Aiym Kereikulova); resources, Y.B. and A.T.; data curation, A.K. (Aiym Kereikulova); writing—original draft preparation, A.K. (Aiym Kereikulova) and Y.B.; writing—review and editing, A.K. (Abdelhamid Kheiri), M.K., O.B., and Y.B.; visualization, A.K. (Aiym Kereikulova) and Y.Y.; supervision, Y.B. and A.T. All authors have read and agreed to the published version of the manuscript.

Funding: This research received no external funding.

Data Availability Statement: The data presented in this study are available on request from the corresponding author.

Acknowledgments: The authors express their sincere gratitude to the "Heat Management" research team at the LEMTA R&D Center of the University of Lorraine and CNRS (Nancy, France) for their valuable support. The authors also acknowledge the organizers of the double-degree Master's program between Al-Farabi Kazakh National University (Kazakhstan) and the University of Lorraine (France), specializing in "7M05405—Mechanics and Energy," for their contribution to the academic preparation of Master's graduates. The authors are particularly grateful to Olivier Botella for his supervision of Master's student Aiym Kereikulova in CFD modeling of high-temperature thermal storage in a PCM tank.

Conflicts of Interest: The authors declare no conflicts of interest.

Abbreviations

The following abbreviations are used in this manuscript:

CSP	Concentrated solar power
HVAC	Heating, Ventilation and Air Conditioning
TES	Thermal energy storage
PCMs	Phase change materials
HTF	Heat transfer fluid

Nomenclature

$\vec{u}$	Velocity vector, m/s
u_{in}	Inlet velocity, m/s
Q	Mass flow rate, kg/s
C_p	Heat capacity, J/kg K
T	Temperature, K
T^*	Dimensionless temperature [-]
T_h	Hot water temperature, K
T_c	Cold water temperature, K
T_a	Ambient temperature, K
T_{out}	Outlet temperature, K
a	Diameter of holes (shower inlet), m
b	Groove width (groove inlet), m
k	Thermal conductivity, W/mK
E_{stored}	Stored energy, J
$E_{\max_stored}$	Maximum storage capacity, J
E_i	Energy of i-th layer, J
t_x	Time moment, s
t	Time, s
t^*	Dimensionless time [-]
Δz	Layer width, m
E	Energy, J
M_E	Thermal momentum, J·m
P	Pressure, Pa
β	Coefficient of thermal expansion, 1/K
ρ	Density, kg/m^3
ρ_0	Reference density (kg/m^3)
ϑ	Kinematic viscosity, m^2/s
ε	Tail factor [-]
D	Diameter of tank, m
H	Height of tank, m
V	Volume, m^3
V_i	Volume of i-th layer, m^3
V_{tank}	Tank volume, m^3
MIX	Mix number [-]
Str	Stratification number [-]
σ	Capacity ratio [-]
η	Exergy efficiency [-]
S	Suraface area of tank, m^2
N	Number of orifices [-]

References

1. Zhang, H.; Baeyens, J.; Cáceres, G.; Degrève, J.; Lv, Y. Thermal energy storage: Recent developments and practical aspects. *Prog. Energy Combust. Sci.* **2016**, *53*, 1–40. [CrossRef]
2. Pelay, U.; Luo, L.; Fan, Y.; Stitou, D.; Castelain, C. Integration of a thermochemical energy storage system in a Rankine cycle driven by concentrating solar power: Energy and exergy analyses. *Energy* **2019**, *167*, 498–510. [CrossRef]
3. Pelay, U.; Luo, L.; Fan, Y.; Stitou, D.; Rood, M. Thermal energy storage systems for concentrated solar power plants. *Renew. Sustain. Energy Rev.* **2017**, *79*, 82–100. [CrossRef]
4. Li, G. Sensible heat thermal storage: Energy and exergy performance evaluations. *Renew. Sustain. Energy Rev.* **2016**, *53*, 897–923. [CrossRef]
5. Karim, A.; Burnett, A.; Fawzia, S. Investigation of Stratified Thermal Storage Tank Performance for Heating and Cooling Applications. *Energies* **2018**, *11*, 1049. [CrossRef]
6. Chen, X.; Zhai, X.; Wang, R. Thermal performance analysis of a packed bed cold storage unit using composite PCM capsules for high temperature solar cooling application. *Appl. Therm. Eng.* **2016**, *100*, 247–255. [CrossRef]
7. Altuntop, N.; Zilik, Z.; Oezcan, V.; Kincay, O. Effect of Water Inlet Velocity on Thermal Stratification in a Mantled Hot Water Storage Tank. *Int. J. Energy Res.* **2006**, *30*, 163–176. [CrossRef]
8. Davidson, J.H.; Adams, M.W. Fabric stratification manifolds for solar water heating. *J. Sol. Energy Eng.* **1994**, *116*, 130–136. [CrossRef]
9. Wu, F.; Wang, Z.; Zhang, H.; Qin, Y.; You, X.; Lu, J. Experimental and simulation analysis on thermal stratification characteristics in solar storage tanks with phase change materials. *J. Energy Storage* **2022**, *46*, 103722. [CrossRef]
10. Zachar, A.; Farkas, I.; Szlivka, F. Numerical Analyses of the Impact of Plates for Thermal Stratification inside a Storage Tank with Upper and Lower Inlet Flows. *Sol. Energy* **2003**, *74*, 287–302. [CrossRef]
11. Abdidin, A.; Kereikulova, A.; Toleukhanov, A.; Botella, O.; Kheiri, A.; Belyayev, Y. Two-dimensional CFD analysis of a hot water storage tank with immersed obstacles. *J. Math. Mech. Comput. Sci.* **2024**, *123*, 57–80. [CrossRef]
12. Li, S.-H.; Zhang, Y.-X.; Li, Y.; Zhang, X.-S. Experimental study of inlet structure on the discharging performance of a solar water storage tank. *Energy Build.* **2014**, *70*, 490–496. [CrossRef]
13. Shah, L.J.; Furbo, S. Entrance effects in solar storage tanks. *Solar Energy* **2003**, *75*, 337–348. [CrossRef]
14. Shah, L.J.; Furbo, S. Correlation of Experimental and Theoretical Heat Transfer in Mantle Tanks Used in Low-Flow Solar Domestic Hot Water Systems. *Solar Energy* **1998**, *64*, 245–256. [CrossRef]
15. Manu, K.V.; Anand, P.; Chetia, U.K.; Basu, S. Effects of instabilities and coherent structures on the performance of a thermocline based thermal energy storage. *Appl. Therm. Eng.* **2015**, *87*, 768–778. [CrossRef]
16. Shafieian, A.; Bahrami, H.-R.; Roostaee, A.; Feyzi, S.S. Effects of different inlet configurations on the performance of solar storage tanks: A three-dimensional unsteady CFD simulation. *Case Stud. Therm. Eng.* **2023**, *45*, 103019. [CrossRef]
17. Abdidin, A.; Seitov, A.; Toleukhanov, A.; Belyayev, Y.; Botella, O.; Kheiri, A.; Khalij, M. Three-dimensional CFD analysis of a hot water storage tank with various inlet/outlet configurations. *Energies* **2024**, *17*, 5716. [CrossRef]
18. Rojas, E.; Alonso, E.; Rodriguez-Garcia, M.; Bayon, R.; Avila-Marin, A. Characterization by key performance indicators of SFERA-III project to ALTAYR packed-bed prototype. *Appl. Energy* **2025**, *377*, 124590. [CrossRef]
19. Sougtan, Y.; Khalij, M.; El Qarnia, H.; Kheiri, A. Rock bed thermal energy storage with thermocline: The effect of rock arrangement structure on heat storage performances. *J. Energy Storage* **2020**, *100*, 70134. [CrossRef]
20. Nandi, B.R.; Bandyopadhyay, S.; Banerjee, R. Numerical modeling and analysis of dual medium thermocline thermal energy storage. *J. Energy Storage* **2018**, *16*, 218–230. [CrossRef]
21. Xia, L.; Zhang, P.; Wang, R.Z. Numerical heat transfer analysis of the packed bed latent heat storage system based on an effective packed bed model. *Energy* **2010**, *35*, 2022–2032. [CrossRef]
22. Ismail, K.A.R.; Stuginsky, R., Jr. A parametric study on possible fixed bed models for PCM and sensible heat storage. *Appled Therm. Eng.* **1999**, *19*, 757–788. [CrossRef]
23. Wang, Z.; Zhang, H.; Dou, B.; Zhang, G.; Huang, H. The thermal stratification evaluation of phase-change materials in a heat storage tank: Computational fluid dynamics and experimental study. *J. Sol. Energy Eng.* **2020**, *142*, 021012. [CrossRef]
24. Bayón, R.; Rojas, E. Simulation of thermocline storage for solar thermal power plants: From dimensionless results to prototypes and real-size tanks. *Int. J. Heat Mass Transf.* **2013**, *60*, 713–721. [CrossRef]
25. Lou, W.; Luo, L.; Hua, Y.; Fan, Y.; Du, Z. A review on the performance indicators and influencing factors for thermocline thermal energy storage systems. *Energies* **2021**, *14*, 8384. [CrossRef]

26. Lou, W.; Fan, Y.; Luo, L. Single-tank thermal energy storage systems for concentrated solar power: Flow distribution optimization for thermocline evolution management. *J. Energy Storage* **2020**, *32*, 101749. [CrossRef]
27. Wang, Z.; Zhang, H.; Dou, B.; Zhang, G.; Wu, W.; Zhou, L. An experimental study for the enhancement of stratification in a heat-storage tank by equalizer and PCM module. *J. Energy Storage* **2020**, *27*, 101010. [CrossRef]

Disclaimer/Publisher's Note: The statements, opinions and data contained in all publications are solely those of the individual author(s) and contributor(s) and not of MDPI and/or the editor(s). MDPI and/or the editor(s) disclaim responsibility for any injury to people or property resulting from any ideas, methods, instructions or products referred to in the content.